Check for updates

A Novel Application of Radiomics Analysis for Computational Fluid Dynamics Evaluation of Cerebral Aneurysms

Alexandra Lauric and Adel M. Malek

■ BACKGROUND: **PyRadiomics is a recently introduced automatic imaging tool for evaluating intensity-based texture descriptors and shape morphology. Due to intensity homogeneity in contrast-enhanced rotational angiography, radiomics analysis for intracranial aneurysms was previously limited to morphological evaluation. We propose a novel use of radiomics analysis to assess aneurysm intradome velocity distributions derived from computational fluid dynamics (CFD) simulations.**

■ METHODS: **Catheter 3D rotational angiographic volumes from 68 aneurysms (29 ruptured) were analyzed. Steady-state CFD simulations were performed on segmented models, and intra-dome velocity distributions were extracted using mesh-independent isometric sampling. Velocity volumes were normalized for size and magnitude, converted to grayscale DICOM, and analyzed to extract 93 histogram and texture radiomics features. Uni- and multivariate analyses assessed these features for rupture status discrimination.**

■ RESULTS: **Radiomics analysis showed that ruptured aneurysms had significantly lower energy ($P = 0.005$) and entropy ($P = 0.004$), but higher skewness ($P = 0.001$), kurtosis ($P < 0.001$), and uniformity ($P = 0.001$) than unruptured ones. Texture analysis revealed lower contrast ($P = 0.02$) and gray-level variance ($P = 0.02$), but higher strength ($P = 0.04$). Ruptured aneurysms also showed greater clustering of low gray-level values, reflected by higher LowGrayLevelEmphasis ($P = 0.001$) and LargeAreaLowGrayLevelEmphasis ($P = 0.01$). Multivariate analysis achieved an AUC of 0.90 (sensitivity 0.86, specificity 0.85).**

■ CONCLUSION: **Automatic histogram and texture analysis of intra-dome velocity using radiomics showed strong rupture status discrimination. Ruptured aneurysms exhibited pattern uniformity with reduced gray-level variability, and fewer high-intensity areas. This novel approach to CFD volumetric evaluation, extending radiomics use beyond angiographic analysis, provides insights into rupture characteristics, and opens novel and promising avenues of future research.**

INTRODUCTION

PyRadiomics,[1] an automatic image processing tool, has been recently proposed for intracranial aneurysms morphological evaluation.[2-5] While the risk of rupture for

Key words
- Computational fluid dynamics
- Intracranial aneurysms
- Radiomics
- Ruptured status
- Velocity texture

Abbreviations and Acronyms
AR: Aspect ratio
AUC: Area under the curve
CFD: Computational fluid dynamics
Dmax: Maximum diameter
GLCM: Gray level co-occurrence matrix
GLDM: Gray level dependence matrix
GLRLM: Gray level run length matrix
GLSZM: Gray level size zone matrix
Hmax: Maximum height
HW: Height-to-width ratio
MRA: Magnetic resonance angiography
MRI: Magnetic resonance imaging
NGTDM: Neighboring gray tone difference matrix
NSI: Non-sphericity index
ROC: Receiver operating characteristic
SR: Rize ratio
WSS: Wall shear stress

Cerebrovascular Hemodynamics Laboratory, Department of Neurosurgery, Tufts Medical Center and, Tufts University School of Medicine, Boston, MA, USA

To whom correspondence should be addressed: Adel M. Malek, M.D., Ph.D. [E-mail: amalek@tuftsmedicalcenter.org]

Supplementary digital content available online.

Citation: World Neurosurg. (2026) 205:124602. http://doi.org/10.1016/j.wneu.2025.124602

*Journal homepage: **www.journals.elsevier.com/world-neurosurgery***

*Available online: **www.sciencedirect.com***

1878-8750/© 2025 The Author(s). Published by Elsevier Inc. This is an open access article under the CC BY license (http://creativecommons.org/licenses/by/4.0/).

cerebral aneurysms is relatively low,[6,7] when occurring, aneurysmal subarachnoid hemorrhage still carries high mortality and morbidity rates.[8] Consequently, the ability to understand the mechanisms for aneurysmal rupture and to evaluate rupture risk, particularly in an automatic fashion, is of high clinical value.

Radiomics allows for the evaluation of both shape morphology, and intensity-based descriptors (histogram, texture, and patterns). Previously, these features were evaluated for shape and image analysis of pathological lesions, such as lung cancer,[9] liver fibrosis,[10] prostate lesions,[11] glioblastoma,[12] and metastatic brain tumors,[13] and metastases to the head and neck.[14] In addition, radiomics descriptors were previously used for angiographic parametric imaging analysis as biomarkers related to blood flow contrast in the aneurysmal sac[15] and for the prediction of aneurysm occlusion pre- and post-intervention.[16]

Cerebral aneurysms are often evaluated using catheter 3D rotational angiography. Because of intensity homogeneity due to contrast-enhanced imaging, evaluation of intensity texture and patterns were not applicable for these volumes. Because of this, radiomics-derived morphological descriptors have been previously mostly evaluated for rupture risk stratification of cerebral aneurysms.[2-5] More recent research has proposed radiomics texture pattern analysis on magnetic resonance angiographic aneurysmal data.[17]

In addition to morphology, hemodynamics are considered a major contributor to aneurysm formation and rupture[18]; research has focused on wall shear stress (WSS), the tangential force of flowing blood on the vessel surface. In contrast, volumetric analysis for rupture risk includes evaluation of flow pattern[19] and flow instability,[20] with velocity patterns often used for visualization purposes and qualitative analysis. This retrospective study proposes an in-depth evaluation of aneurysm intra-dome velocity distributions by use of radiomics histogram and texture analysis—a novel application of radiomics to the field of computation fluid dynamics.

MATERIALS AND METHODS

Patient Selection

Sixty-eight high-resolution 3-dimensional catheter angiographic volumetric datasets were available from patients with intracranial aneurysms (29 ruptured). All imaging of the ruptured subset was obtained within 48 hours from rupture to avoid vasospasm onset. This research was approved by the Institutional Review Board ethics committee. Patient consent was waived because of the retrospective nature of the study not impacting patient clinical care.

Cerebral Angiography and Data Processing

Three-dimensional catheter-based cerebral angiograms were obtained using a calibrated biplane system, with volume reconstruction using the available clinical software package, to yield a three-dimensional volumetric dataset. Volumes were processed and analyzed using Amira visualization software platform version 5.3.3 (FEI, Hillsboro, OR) for segmentation of aneurysm and surrounding vessel in three-dimensional space (**Figure 1A**). From each aneurysm, morphological features including maximum diameter (Dmax), maximum height (Hmax), height-to-width ratio (HW), aspect ratio (AR), size ratio (SR), and non-sphericity index (NSI) were computed as described in the literature.[5]

Segmented models were used to create dynamic tetrahedral/prismatic meshes with boundary layer enhancement using ICEM CFD meshing (Ansys 19.2, Ansys Inc., Lebanon, NH). The segment proximal to the site of the aneurysm was kept sufficiently long (at least 5 times the diameter of the parent vessel) in order to enable the laminar flow to become fully developed and avoid entrance effects.[21]

Computational Fluid Dynamics

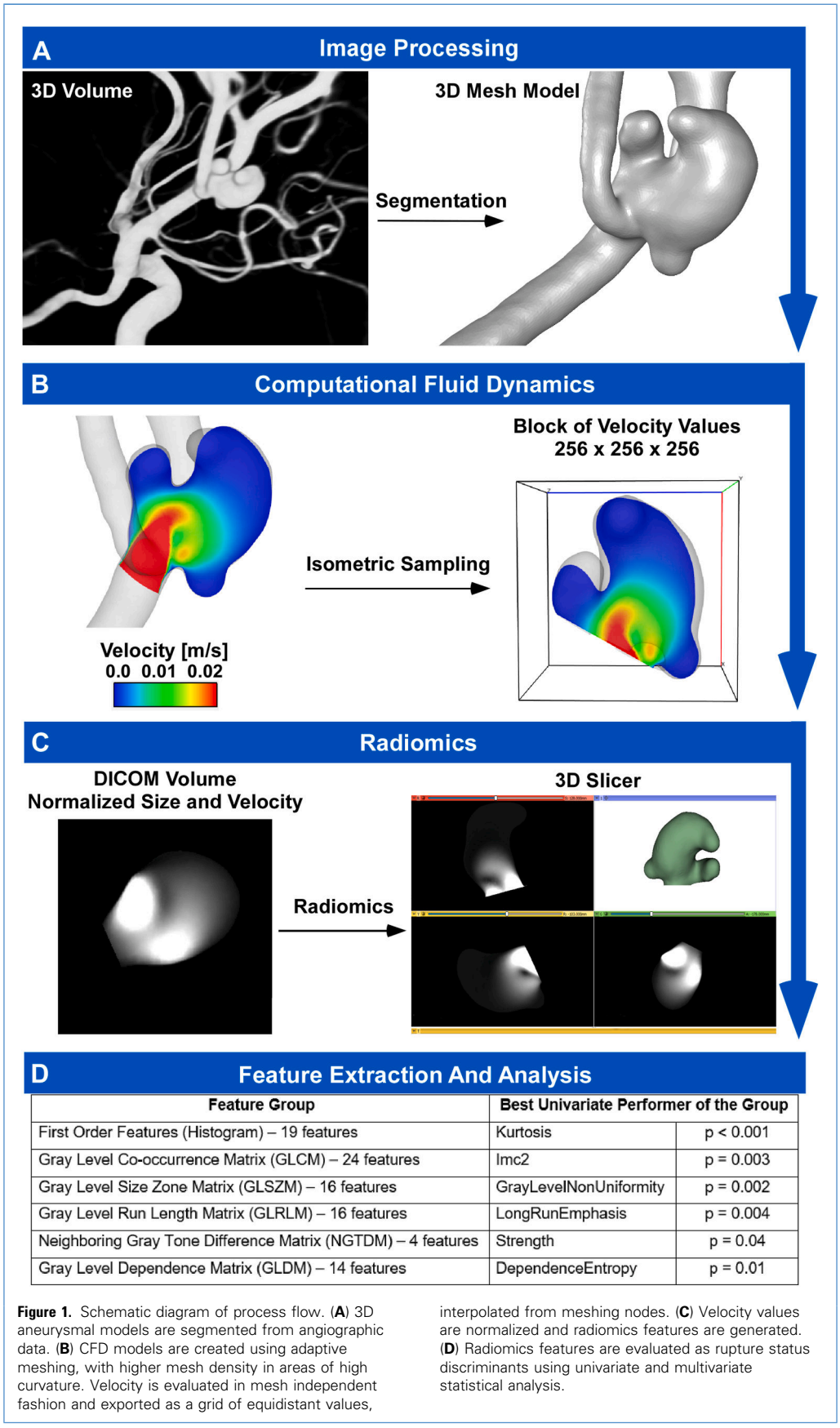
Computational fluid dynamics (CFD) simulations were performed using Ansys Fluent 19.2 (Ansys Inc., Labanon, NH), by modeling steady state laminar flow with a Carreau non-Newtonian profile to better approximate the viscosity and flow of blood.[22] In order to account for variability in the size, shape, and length of the parent vessel, flow scaling factors were determined for each model to ensure ideal parent vessel WSS conditions of approximately 1.5 Pa at parent vessel proximal to the aneurysm. Subsequently, steady flow was applied at the inlet according to the resulting scaled velocity, with zero-gauge pressure at the outlets.

Post-processing analysis was performed using EnSight 10.2 (Ansys Inc., Labanon, NH). The aneurysm dome was separated from surrounding vessels, and velocity values were exported using the "Brick of Values" export option, creating an isotropic discretization of the volume of interest (**Figure 2B**). Velocity volumes were exported as a $256 \times 256 \times 256$ grid of equidistant float values, interpolated from meshing nodes. The resulting mean voxel resolution for the entire aneurysmal set was 0.033 ± 0.01 mm. This isometric sampling approach avoids the pitfalls of enriching velocity values in regions of higher mesh density. Following EnSight export and prior to radiomics evaluation, volumes were normalized for size to unit cube and for velocity to the [0, 1] range. Grayscale DICOM volumes were created by multiplying the normalized velocity by 1000, bringing the intensity range to [0, 1000].

Radiomics and Feature Extraction

Radiomics is an advanced image-analysis technique that extracts a large number of quantitative descriptors from imaging data, features which are not visually discernible.[23] Rather than relying on subjective visual assessment, radiomics uses computational algorithms to evaluate the distribution of intensities, the spatial relationships of voxel values that reflect texture, and shape-related characteristics of anatomical structures. These features are standardized, automatically computed, and reproducible, allowing comparisons across patients and datasets. In the context of aneurysm research, radiomics transforms complex hemodynamic or morphological data into a set of measurable features that can then be systematically correlated with rupture status.

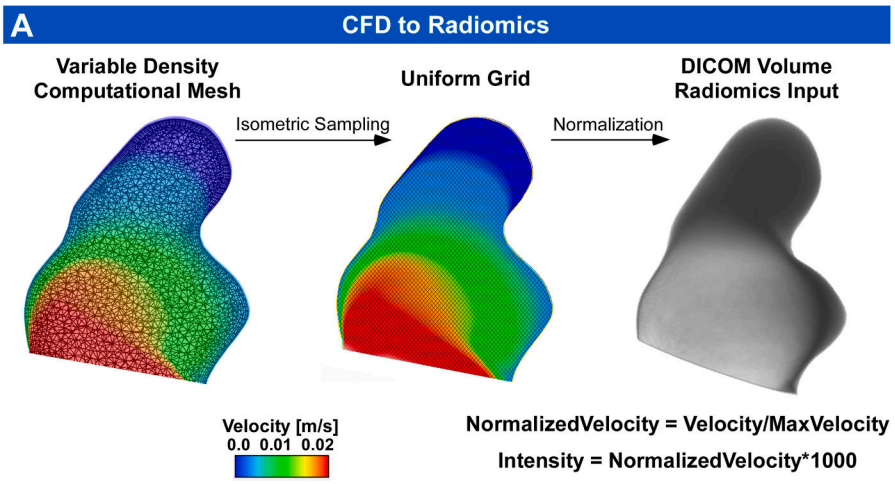
PyRadiomics package,[1] implemented in Python, and integrated into the 3D Slicer platform,[24] was used (**Figure 1C**). PyRadiomics features are organized in 8 groups: 2D Shape Features, 3D Shape Features, First Order Features, Gray Level Co-occurrence Matrix Features (GLCM), Gray Level Size Zone Matrix Features (GLSZM), Gray Level Run Length Matrix Features (GLRLM), Neighboring Gray Tone Difference Matrix Features (NGTDM), and Gray Level Dependence Matrix Features (GLDM). The use of radiomics

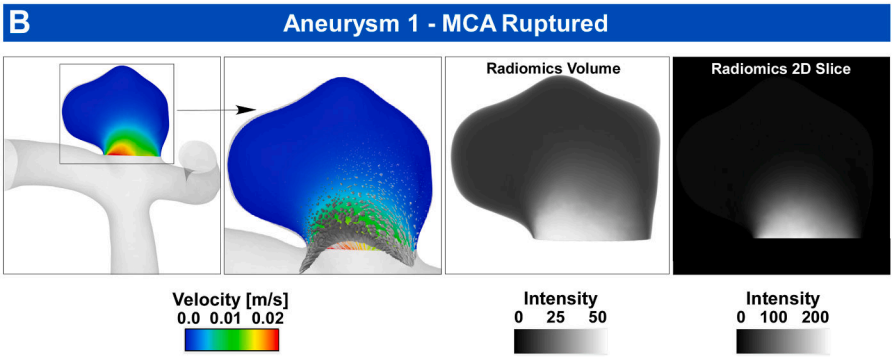


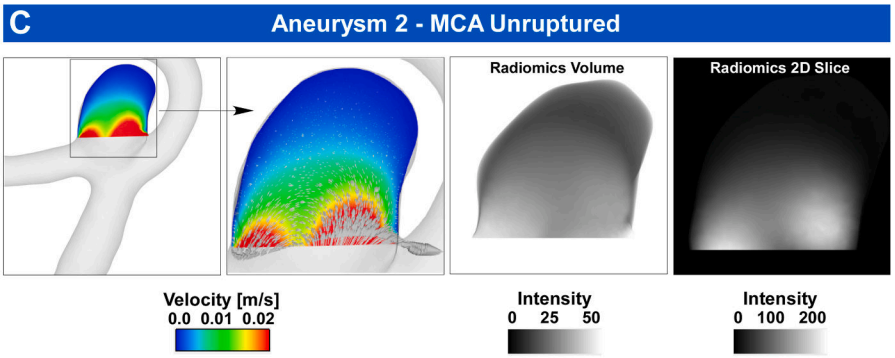
D Feature Extraction And Analysis

Feature Group	Best Univariate Performer of the Group	
First Order Features (Histogram) – 19 features	Kurtosis	p < 0.001
Gray Level Co-occurrence Matrix (GLCM) – 24 features	Imc2	p = 0.003
Gray Level Size Zone Matrix (GLSZM) – 16 features	GrayLevelNonUniformity	p = 0.002
Gray Level Run Length Matrix (GLRLM) – 16 features	LongRunEmphasis	p = 0.004
Neighboring Gray Tone Difference Matrix (NGTDM) – 4 features	Strength	p = 0.04
Gray Level Dependence Matrix (GLDM) – 14 features	DependenceEntropy	p = 0.01

Figure 1. Schematic diagram of process flow. (**A**) 3D aneurysmal models are segmented from angiographic data. (**B**) CFD models are created using adaptive meshing, with higher mesh density in areas of high curvature. Velocity is evaluated in mesh independent fashion and exported as a grid of equidistant values, interpolated from meshing nodes. (**C**) Velocity values are normalized and radiomics features are generated. (**D**) Radiomics features are evaluated as rupture status discriminants using univariate and multivariate statistical analysis.







D Feature Comparison Aneurysm 1 vs. Aneurysm 2

Histogram Features		Texture Features	
Aneurysm 1 (ruptured)	**Aneurysm 2 (unruptured)**	**Aneurysm 1 (ruptured)**	**Aneurysm 2 (unruptured)**
Total Energy = 3353	Total Energy = 7680	Strength = 0.172	Strength = 0.076
Entropy = 2.18	Entropy = 3.54	Contrast = 0.0009	Contrast = 0.0028
Kurtosis = 19.9	Kurtosis = 9.91	Complexity = 64.7	Complexity = 114.7
Skewness = 3.68	Skewness = 2.24	GrayLevelVariance = 14.77	GrayLevelVariance = 23.34
Uniformity = 0.42	Uniformity = 0.12	HighGrayLevelEmphasis = 22.06	HighGrayLevelEmphasis = 46.93
		LowGrayLevelEmphasis = 0.67	LowGrayLevelEmphasis = 0.31

Figure 2. (**A**) Mesh independent intra-dome velocity values are normalized and converted to grayscale DICOM volumes. (**B**) Aneurysm 1—velocity detail for a ruptured MCA aneurysm. Detail to velocity distribution and corresponding Radiomics volume. (**C**) Aneurysm 2—velocity detail for an unruptured MCA aneurysm. (**D**) Feature comparison between Aneurysm 1 and Aneurysm 2. Histogram-wise, the ruptured aneurysm has higher kurtosis, skewness, and uniformity, but lower energy and entropy. Texture-wise the ruptured aneurysm has higher Strength and LowGrayLevelEmphasis, but lower Contrast and GrayLevelVariance.

morphological features for rupture status discrimination was previously discussed[3,5] and was not evaluated here. This study focuses on histogram descriptors (first order features) and on gray level texture features. First order features describe the distribution of voxel intensities within the volume. Texture and pattern features provide information regarding the relative position of voxels in the volume, and their relationship with neighboring voxels. A complete list of radiomics features evaluated in this study is available in **Supplementary Table 1**.

First Order Features (19 features) describe the histogram of the intensity voxels and includes descriptors such as: energy, moments of the distribution, entropy, etc.

Gray Level Co-occurrence Matrix Features (GLCM—24 features) quantify the number of times two intensities in the image occur within a specified distance and at a specific angle. The group includes descriptors such as Correlation, ClusterProminence, ClusterShade, Contrast, and so on.

Gray Level Size Zone Matrix Features (GLSZM—16 features) quantify the gray level zones in the image. A gray level zone is defined as a number of connected voxels (26-connected region) that have the same intensity. The group includes descriptors such as GrayLevelVariance, ZoneVariance, ZoneEntropy, SizeZoneNonUniformity, and so on.

Gray Level Run Length Matrix Features (GLRLM—16 features) quantify gray level runs. Intensity runs are defined as the length of consecutive voxels that have the same gray level value. The group includes descriptors such as RunPercentage, RunVariance, RunEntropy, RunLengthNonUniformity, LowGrayLevelRunEmphasis, HighGrayLevelRunEmphasis, and so on.

Neighboring Gray Tone Difference Matrix Features (NGTDM—5 features) quantify the difference between a gray value and the average gray value of its neighbors. The group descriptors are Coarseness, Contrast, Busyness, Complexity, and Strength.

Gray Level Dependence Matrix Features (GLDM—14 features) quantify gray level dependencies in the image. A gray level dependency is defined as the number of connected voxels within a specific distance that are dependent on the center voxel (their intensities are within a certain threshold). The group includes descriptors such as SmallDependenceEmphasis, LargeDependenceEmphasis, DependenceNonUniformity, DependenceVariance, DependenceEntropy, and so on.

Detailed information regarding all radiomics features is available in the PyRadiomics documentation (http://PyRadiomics.readthedocs.io/en/latest/) and in the work of Scapicchio et al.[23]

Statistical Analysis

JMP statistical software (Version Pro 17, SAS Institute, Cary, NC) was used to evaluate the performance of all Radiomics features in discriminating between ruptured and unruptured aneurysms using the student t-test analysis with statistical significance assumed for $P < 0.05$. Receiver operating characteristics curve (ROC) analysis was performed, and prediction accuracy evaluated using the area under the curve (AUC) index, including sensitivity and specificity metrics. The R-squared coefficient of determination is evaluated for feature dependency analysis.

Multivariate logistic regression was performed using elastic net regularization to mitigate overfitting and address potential correlations among radiomics features. Separate analyses were conducted for morphological and radiomics parameters. Feature selection was integrated within the elastic net framework, using 5-fold cross-validation to promote model robustness and generalizability. Only features with non-zero coefficients were retained as predictive variables in the final model. To ensure model simplicity and avoid overfitting, the number of covariates was limited to a maximum of 5.

RESULTS

Patient Demographics

3D rotational angiographic datasets from 68 patients (29 ruptured, 56 women) harboring intracranial aneurysms were analyzed for the study. It should be noted that the relatively larger proportion of females in our dataset reflects the fact that female sex is associated with a greater prevalence of cerebral aneurysms,[25] and with a greater risk of aneurysmal rupture.[26] Aneurysms in the dataset originated from the internal carotid artery (32%), middle cerebral artery (32%), and posterior communication artery (36%), with 52% classified as sidewall and 48% as bifurcation. There was no statistically significant age difference between patients with ruptured versus unruptured aneurysms (61.82 ± 11.52 vs. 59.28 ± 12.75 years, $P = 0.39$).

Morphological Feature Analysis

Univariate statistical analysis of established size and shape descriptors revealed significantly higher values for ruptured aneurysms across all parameters. Maximum diameter (Dmax), maximum height (Hmax), height/width ratio, aspect ratio, size ratio, and the non-sphericity index (NSI) were significantly elevated in the ruptured group ($P < 0.05$ for all). AUC values ranged from 0.64 to 0.82, with the highest discrimination achieved by aspect ratio and size ratio (AUC = 0.82).

Radiomics Analysis

Although radiomics generates a large number of features, there are many dependencies between pairs of descriptors. Univariate statistical analysis and feature dependence evaluations were performed for each of the feature groups. Complete list of univariate analysis for all radiomics features generated in this study is available as **Supplementary Table 1**. Univariate statistical analysis for the best performing features within each group is available in **Table 1**.

First Order Features

As shown in **Table 1**, ruptured aneurysms had significantly lower Energy ($P = 0.005$) and TotalEnergy ($P = 0.005$) compared to unruptured aneurysms. Energy is a measure of voxel magnitude in the volume and lower values suggest a concentration of low velocity values in ruptured aneurysms.

Dependencies were observed between Total Energy and Entropy ($P < 0.001$, $R^2 = 0.52$), Mean ($P < 0.001$, $R^2 = 0.76$), Root Mean Squared ($P < 0.001$, $R^2 = 0.76$), Interquartile Range ($P < 0.001$, $R^2 = 0.53$), and Mean Absolute Deviation ($P < 0.001$, $R^2 = 0.51$).

Skewness and Kurtosis, the other strong discriminants in this group, were only weakly correlated with Total Energy. Ruptured aneurysms have significantly larger skewness (2.56 ± 1.24 vs. 1.68 ± 0.86, $P = 0.001$) and kurtosis (13.41 ± 9.39 vs. 6.99 ± 4.64, $P < 0.001$) compared to unruptured aneurysms. Skewness

describes the extent of asymmetry in the shape of a distribution, with positive skewness indicating a distribution concentrated on smaller values. Kurtosis describes the tails of a distribution. A normal distribution has a kurtosis of 3, whereas an exponential distribution has a kurtosis of 9. Kurtosis values larger than 3 (leptokurtic distributions) describe distributions with longer tails and more outliers compared to normal distributions. Skewness and Kurtosis were highly dependent variables ($P < 0.001$, $R^2 = 0.98$), as were the Skewness and Uniformity ($P < 0.001$, $R^2 = 0.71$).

Gray Level Co-occurrence Matrix Features

Ruptured aneurysms had significantly lower Imc2 (informational measure of correlation, $P = 0.003$) and MCC (maximum correlation coefficient, $P = 0.003$) compared to unruptured aneurysms. These are measures which quantify the correlation between adjacent voxels and describe the complexity of the image texture, with lower values suggesting less complexity and texture structure. This is further emphasized by lower ClusterTendency ($P = 0.01$) in ruptured aneurysms.

Table 1. Univariate Statistical Analysis of High Performance Radiomics Descriptors for Rupture Status Discrimination

Radiomics Descriptors	Ruptured	Unruptured	*P* Value	AUC
First Order Features				
Energy	130610000000 ± 104150000000	218520000000 ± 136010000000	0.005	0.73
Entropy	3.3984 ± 1.0794	4.0616 ± 0.74751	0.004	0.69
Kurtosis	13.416 ± 9.3984	6.9904 ± 4.6434	<0.001	0.76
Skewness	2.5604 ± 1.2408	1.6821 ± 0.86217	0.001	0.73
Total Energy	8359.2 ± 6665.8	13985 ± 8704.4	0.005	0.73
Uniformity	0.21933 ± 0.17688	0.11478 ± 0.096691	0.003	0.69
Variance	18202 ± 10097	27276 ± 11046	0.001	0.73
Gray level co-occurrence matrix				
Cluster Tendency	145.61 ± 105.6	210.16 ± 104.24	0.014	0.69
Correlation	0.99524 ± 0.002967	0.99674 ± 0.001325	0.006	0.71
Imc2	0.99341 ± 0.009530	0.99826 ± 0.002512	0.003	0.78
MCC	0.99604 ± 0.002194	0.99728 ± 0.001018	0.003	0.73
Gray level size zone matrix features				
GrayLevelNonUniformity	731,110 ± 675,230	389,000 ± 355,020	0.009	0.66
GrayLevelVariance	37.001 ± 27.065	53.272 ± 26.614	0.02	0.69
ZoneVariance	10,502,000,000 ± 17,808,000,000	2,704,100,000 ± 4,448,300,000	0.01	0.59
LargeAreaEmphasis	10,719,000,000 ± 18,276,000,000	2781000000 ± 4,509,700,000	0.01	0.58
LargeAreaLowGrayLevelEmphasis	6,193,400,000 ± 13017000000	924,790,000 ± 2,150,600,000	0.02	0.60
Gray level run length matrix features				
LongRunLowGrayLevelEmphasis	148.56 ± 218.62	45.983 ± 77.713	0.008	0.64
LowGrayLevelRunEmphasis	0.14154 ± 0.07783	0.10726 ± 0.04795	0.03	0.64
RunVariance	214.63 ± 229.09	88.337 ± 101.95	0.003	0.66
Neighbouring gray tone difference matrix features				
Contrast 2	0.0059038 ± 0.0061708	0.0094728 ± 0.0063897	0.02	0.70
Strength	0.1357 ± 0.08193	0.095667 ± 0.07566	0.04	0.71
Gray level dependence matrix features				
DependenceEntropy	6.1967 ± 2.0974	7.3299 ± 1.4636	0.01	0.67
LowGrayLevelEmphasis	0.28724 ± 0.21375	0.1933 ± 0.14518	0.04	0.62
SmallDependenceLowGrayLevelEmphasis	0.00172 ± 0.001330	0.00154 ± 0.001276	0.02	0.68

Shown are mean and standard deviation. Statistical significance was assumed for $P < 0.05$. AUC represents the area under the ROC curve. Only statistically significant features were included.

Gray Level Size Zone Matrix Features

This group of features quantify regions of connected voxels with the same intensity. Ruptured aneurysm have smaller GrayLevelVariance ($P = 0.02$) and are characterized by larger connected regions (larger LargeAreaEmphasis, $P = 0.01$) in the low gray level value range (larger LargeAreaLowGrayLevelEmphasis, $P = 0.02$). However, within the lower gray level values there was higher GrayLevelNonUniformity ($P = 0.009$) and higher ZoneVariance ($P = 0.01$) in ruptured aneurysms.

Gray Level Run Length Matrix Features

Image runs are defined as the length of consecutive voxels that have the same gray level value. RunVariance, the variance of run lengths, was significantly larger in ruptured compared to unruptured aneurysms ($P = 0.003$) suggesting higher gray level homogeneity in ruptured aneurysms. In addition, LongRunLowGrayLevelEmphasis ($P = 0.008$), a measure of the distribution of long run lengths with lower gray-level values, was also significantly higher in ruptured aneurysms, as was LowGrayLevelRunEmphasis ($P = 0.003$), suggestive of long strands of low velocity values.

Neighboring Gray Tone Difference Matrix Features

Image Strength was significantly larger in ruptured aneurysms compared to unruptured ($P = 0.04$). However, Contrast was significantly smaller in ruptured aneurysms ($P = 0.02$). This suggests that ruptured aneurysms have well defined image primitive (image components such as focal intensity points), but a low range of gray levels with low spatial intensity change.

Gray Level Dependence Matrix Features

Features in this group quantify voxel intensity dependencies in an image within a particular size neighborhood. DependenceEntropy was significantly smaller in the ruptured group compared to unruptured, indicating a lower concentration of high gray-level values in the ruptured volumes, with larger dependencies in the low gray level range (larger LowGrayLevelEmphasis, and larger SmallDependenceLowGrayLevelEmphasis).

Multivariate Analysis

Elastic net regression with 5-fold cross-validation identified five velocity-based radiomics features as independent predictors of rupture status: Coarseness, Strength, Imc1, Skewness, and GrayLevelNonUniformity.

Among these, Coarseness (estimate: +24.92), Imc1 (+17.89), Skewness (+16.20), and GrayLevelNonUniformity (+10.72) had positive coefficients, indicating that higher texture coarseness, stronger voxel intensity correlation, greater distribution asymmetry, and higher gray-level non-uniformity are associated with aneurysm rupture. In contrast, Strength (−22.47) had a negative coefficient, suggesting that lower definition of image sub-components is linked to rupture in the presence of these other variables. Strength's negative coefficient in the multivariate model, despite its positive univariate association ($P = 0.04$), likely results from its moderate correlation with Coarseness ($P < 0.001$, $R^2 = 0.38$), indicating that lower Strength reflects fewer high-velocity focal points when controlling for locally uniform texture patterns (high coarseness) in ruptured aneurysms.

The combined multivariate model achieved an AUC of 0.90, with sensitivity of 0.86 and specificity of 0.85. In comparison, the multivariate morphological model achieved an AUC of 0.83, with sensitivity of 0.82 and specificity of 0.79.

DISCUSSION

Radiomics feature extraction has the advantages of automatic and thus reproducible, user-independent, evaluation of morphological and texture characteristics of volumetric images. Radiomics descriptors were previously employed in the study of various types of pathological lesions.[9-14] Specifically, first order distribution derived features were shown to discriminate between benign and malignant prostate lesions.[27] Kurtosis and SmallAreaHighGrayLevelEmphasis (GLSZM feature) were identified as best discriminants of bone lesions in prostate cancer.[28] Energy, Compactness, and GrayLevelNonUniformity were selected in multivariate analysis of the prognostic phenotype in lung and head-and-neck cancer.[29] DependenceVariance and SumEntropy were identified as best predictors of radiotherapeutic response in patients with acromegaly.[30]

In aneurysm evaluation, morphological 2- and 3-dimensional radiomics features had been previously proposed as discriminants of rupture status,[2-5] and their relative usefulness compared to literature-established shape descriptors had been discussed.[3] In contrast, the use of texture and pattern radiomics features for rupture status discrimination is just emerging in the literature.[17]

In addition to morphological evaluation of aneurysmal shapes, CFD simulations are used to provide insight into the mechanisms of aneurysm rupture - surface-based approaches focus on dome WSS statistics, whereas volume-based approaches focus on velocity visualization of flow patterns,[19,31] but less on quantitative analysis based on dome velocity statistics.[32,33] Detmer et al.[32] evaluated mean, peak velocity, and time averaged maximum velocity in the dome, finding higher peak velocities in ruptured cases; similar higher maximum velocity was reported in ruptured lesions by Chung at al.[33] Neither study delved into details of the intra-dome flow velocity distribution. Intra-aneurysmal velocity distribution has been evaluated on 4D phase-contrast MRA imaging[34] showing differences in aneurysm types but not in classifying rupture status.

Here, we propose a novel application of radiomics analysis for the evaluation of aneurysm intra-dome velocity distribution, texture, and patterns. Compared to hemodynamic surface evaluations, volumetric approaches have been previously shown to be more robust to surface irregularities, bleb presence, and artifact noise.[35]

Following CFD simulations, velocity volumes are normalized for size and magnitude, allowing for texture analysis without the compounding effects of size and flow scaling factors. In addition, dome velocity is available for radiomics analysis as a mesh-independent isometric sampling. This is a critical feature of the method as CFD computational meshes and volumes are routinely represented using variable mesh densities, with higher density around areas of curvature and near boundaries, in order to enhance computational efficiency and accuracy. Simply sampling the entirety of these elements would distort the velocity

distribution based on local computational mesh density, limitations which may have hindered prior evaluation attempts.

Radiomics analysis showed high rupture status discriminative performance both in univariate and multivariate analysis and revealed distinct differences between ruptured and unruptured aneurysms. Histogram feature analysis showed that ruptured aneurysms have higher kurtosis (13.4 vs. 6.9), skewness (2.6 vs. 1.7), and uniformity (0.22 vs. 0.11), but lower total energy (8359.2 vs. 13985) and entropy (3.39 vs. 4.06). Velocity moments describe the shape of a distribution, with skewness describing the asymmetry, and kurtosis describing the tails of the distribution. The results show that ruptured aneurysms have exponential velocity distributions (skewness >2 and kurtosis >9) skewed toward low-velocity values. Low energy suggests that ruptured aneurysms have lower overall velocity values, whereas low entropy shows lower value randomness. Texture analysis showed that ruptured aneurysms exhibit higher Strength and LowGrayLevelEmphasis, indicating a stronger presence of texture patterns with lower gray levels. This suggests that ruptured aneurysms tend to have areas with more pronounced variations in intensity (high ZoneVariance) at lower gray levels. On the other hand, ruptured aneurysms show lower Contrast and GrayLevelVariance. This implies that there is less variation in intensity between neighboring voxels, less complexity in the texture patterns, reduced variability in gray levels, and fewer areas with high gray-level intensity.

The multivariate analysis highlights features such as higher coarseness indicating smoother, more homogeneous velocity distributions. The negative coefficient for strength suggests an absence of strong local high-velocity components. Positive skewness reflects distributions dominated by low velocities. Finally, increased gray-level non-uniformity highlights the dominance of clustered low-velocity regions. Altogether, these features collectively support a physiological picture of reduced intra-aneurysmal movement in our cohort of ruptured aneurysms.

The findings that ruptured aneurysms exhibit lower velocities, lower complexity, higher homogeneity, and fewer focal high-velocity points may appear counterintuitive, as prior studies[19,36] often associate rupture with high-velocity jets, complex flow patterns, and instabilities observed in pulsatile flow. Our use of steady-state CFD simulations likely drives these observations, as steady flow averages out temporal variations, emphasizing geometric influences that promote expansive low-velocity stagnation zones in the larger, more irregular domes of ruptured aneurysms. This results in smoother, more homogeneous velocity distributions with fewer high-velocity foci, as inlet momentum diffuses across complex geometries. In contrast, transient (pulsatile) flow captures dynamic features which could increase complexity, velocity, and focal points, aligning with intuitive expectations. However, pulsatile simulations are considerably more time- and resource-intensive, limiting their feasibility in large-scale retrospective studies or clinical settings. A key strength of our approach is demonstrating that steady-state CFD, when coupled with velocity-derived radiomics features, can achieve strong discriminatory performance. Radiomics enables the detection of texture and pattern characteristics that are difficult to discern otherwise and may not have been recognized in prior research. If further validated, this underscores the practical value of steady-state analysis as a scalable and clinically applicable method for rupture risk assessment, while leaving open the possibility that future pulsatile studies could refine and expand upon these findings.

It should be noted that, because this study is retrospective in nature, interpretation of the predictive value of radiomics features assumes that aneurysm surface characteristics do not undergo major changes after rupture, though definitive data remain limited. Prior work supports both perspectives: Asari and Ohmoto[37] identified morphological traits as prospective predictors of rupture risk, suggesting they are intrinsic and present before rupture, while Chien and Sayre[38] documented post-rupture alterations such as curvature changes and bleb formation. Our analysis mitigates this concern by focusing on volumetric velocity-based radiomics features, which are less dependent on surface geometry. Indeed, Lauric et al.[35] showed that intra-dome velocity distributions are more robust to surface irregularities than surface-based measures like wall shear stress, suggesting that velocity-based features may remain stable even in the presence of rupture-related surface changes.

Overall, this novel application of radiomics to CFD volumetric evaluation opens new avenues for future research. Importantly, this methodology can be extended to any volumetric field generated by CFD (such as vorticity, helicity, etc.) and to any imaging modality that provides sufficient aneurysm morphological detail (such as CT, MRI), providing a framework for analyzing complex spatial data. The incorporation of radiomics in CFD evaluation not only enhances our understanding of aneurysmal rupture but also paves the way for further exploration and advancement in this important area of research. These findings will require validation in prospective studies before clinical application in risk assessment of incidental aneurysms.

Study Limitations

The current study represents a retrospective analysis used for classification of previously identified rupture status using velocity-derived radiomics features. It is not intended as a predictive tool for rupture risk. Retrospective analysis depends on the hypothesis that aneurysms do not change size and shape after rupture. Like other retrospective investigations, this design limits our ability to infer causality or to determine whether the observed differences are predictive markers or simply reflect post-rupture changes. Conclusive data on this subject remain to be found, but previous studies have shown that, if post-rupture morphological changes were to occur, volumetric approaches might be robust to these changes.[35]

A further consideration is that validation was limited to internal cross-validation, and no external dataset was available to test generalizability. Model performance was evaluated using internal cross-validation, reporting AUC together with sensitivity and specificity as complementary measures of discriminatory ability. However, without an independent test set, the generalizability of our findings cannot be confirmed. Larger multi-institutional cohorts and independent datasets will be required to establish reproducibility and clinical applicability.

In addition, CFD simulations in this study were performed under steady-state conditions to provide a controlled and reproducible framework. This approach does not account for velocity fluctuations and transient flow patterns that occur under pulsatile conditions. Future studies incorporating pulsatile flow will be important to refine and expand upon the present methodology and determine if steady-state simulations, when combined with velocity-based radiomics capture sufficient discriminatory information needed for rupture risk assessment.

While our findings are promising, this study was designed as a proof of concept focused on introducing in detail the proposed methodology. As this is the first application of radiomics to steady-state velocity fields, the interpretation of individual features remains exploratory and requires further research. Ultimately, the potential of these features to serve as predictive markers can only be confirmed through further validation and prospective studies that evaluate their clinical relevance and practical application in assessing intracranial aneurysms.

CONCLUSION

Radiomics-based histogram and texture analysis of intra-dome velocity strongly discriminated rupture status. Ruptured aneurysms have higher kurtosis, skewness, and uniformity, but lower energy and entropy. Overall ruptured aneurysms were characterized by less variation in intensity between neighboring voxels, less complexity in the texture patterns, reduced variability in gray levels, and fewer areas with high gray-level intensity. These findings suggest ruptured aneurysms are characterized by homogeneous velocity distributions and reduced high-velocity components. Importantly, this methodology can be extended to any volumetric field generated by CFD providing a generalizable framework for analyzing complex spatial data. It provides valuable insights that may be overlooked by conventional processing tools and opens promising avenues of future research and possible applications of radiomics concepts to aneurysm evaluation.

CRediT AUTHORSHIP CONTRIBUTION STATEMENT

Alexandra Lauric: Data curation, Formal analysis, Methodology, Writing — original draft, Writing — review & editing, Software. **Adel M. Malek:** Conceptualization, Data curation, Methodology, Supervision, Writing — review & editing.

REFERENCES

1. van Griethuysen JJM, Fedorov A, Parmar C, et al. Computational radiomics system to decode the radiographic phenotype. *Cancer Res*. 2017;77:e104-e107.
2. Zhang Y, Ma C, Liang S, et al. Morphologic feature elongation can predict occlusion status following pipeline embolization of intracranial aneurysms. *World Neurosurg*. 2018;119:e934-e940.
3. Ludwig CG, Lauric A, Malek JA, Mulligan R, Malek AM. Performance of radiomics derived morphological features for prediction of aneurysm rupture status. *J Neurointerv Surg*. 2020;13:755-761.
4. Liu Q, Jiang P, Jiang Y, et al. Prediction of Aneurysm stability using a machine learning model based on PyRadiomics-Derived morphological features. *Stroke*. 2019;50:2314-2321.
5. Lauric A, Ludwig CG, Malek AM. Enhanced radiomics for prediction of rupture status in cerebral aneurysms. *World Neurosurg*. 2022;159:e8-e22.
6. Wiebers D, Whisnant J, Forbes G, et al. Unruptured intracranial aneurysms—risk of rupture and risk of surgical intervention. *N Engl J Med*. 1998;339:1725-1733.
7. Juvela S, Porras M, Poussa K. Natural history of unruptured intracranial aneurysms: probability of and risk factors for aneurysm rupture. *J Neurosurg*. 2000;93:379-387.
8. van Gijn J, Kerr RS, Rinkel GJE. Subarachnoid haemorrhage. *Lancet*. 2007;369:306-318.
9. Hyun SH, Ahn MS, Koh YW, Lee SJ. A machine-learning approach using PET-based radiomics to predict the histological subtypes of lung cancer. *Clin Nucl Med*. 2019;44:956-960.
10. Wang K, Lu X, Zhou H, et al. Deep learning radiomics of shear wave elastography significantly improved diagnostic performance for assessing liver fibrosis in chronic hepatitis B: a prospective multicentre study. *Gut*. 2019;68:729-741.
11. Toivonen J, Montoya Perez I, Movahedi P, et al. Radiomics and machine learning of multisequence multiparametric prostate MRI: towards improved non-invasive prostate cancer characterization. *PloS one*. 2019;14:e0217702.
12. Fan Y, Chen C, Zhao F, et al. Radiomics-based machine learning technology enables better differentiation between glioblastoma and anaplastic oligodendroglioma. *Front Oncol*. 2019;9:1164.
13. Chen C, Ou X, Wang J, Guo W, Ma X. Radiomics-based machine learning in differentiation between glioblastoma and metastatic brain tumors. *Front Oncol*. 2019;9:806.
14. Zhou Z, Chen L, Sher D, et al. Predicting lymph node metastasis in head and neck cancer by combining many-objective radiomics and 3-dimensioal convolutional neural network through evidential reasoning. *Annu Int Conf IEEE Eng Med Biol Soc*. 2018;2018:1-4.
15. Podgorsak AR, Rava RA, Shiraz Bhurwani MM, et al. Automatic radiomic feature extraction using deep learning for angiographic parametric imaging of intracranial aneurysms. *J Neurointerv Surg*. 2020;12:417-421.
16. Shiraz BMM, Waqas M, Podgorsak AR, et al. Feasibility study for use of angiographic parametric imaging and deep neural networks for intracranial aneurysm occlusion prediction. *J Neurointerv Surg*. 2020;12:714-719.
17. Yamanouchi M, Arimura H, Kodama T, Urakami A. Prediction of intracranial aneurysm rupture risk using non-invasive radiomics analysis based on Follow-Up magnetic resonance angiography images: a preliminary study. *Appl Sci*. 2022;12:8615.
18. Sforza DM, Putman CM, Cebral JR. Hemodynamics of cerebral aneurysms. *Annu Rev Fluid Mech*. 2009;41:91-107.
19. Cebral JR, Castro MA, Burgess JE, Pergolizzi RS, Sheridan MJ, Putman CM. Characterization of cerebral aneurysms for assessing risk of rupture by using patient-specific computational hemodynamics models. *AJNR Am J Neuroradiol*. 2005;26:2550-2559.
20. Valen-Sendstad K, Mardal K-A, Steinman DA. High-resolution CFD detects high-frequency velocity fluctuations in bifurcation, but not sidewall, aneurysms. *J Biomechanics*. 2013;46:402-407.
21. Lauric A, Hippelheuser J, Cohen AD, Kadasi LM, Malek AM. Wall shear stress association with rupture status in volume matched sidewall aneurysms. *J Neurointerv Surg*. 2014;6:466-473.
22. Schirmer CM, Malek AM. Wall shear stress gradient analysis within an idealized stenosis using Non-Newtonian flow. *Neurosurgery*. 2007;61:853-863. ; discussion 863-4.

23. Scapicchio C, Gabelloni M, Barucci A, Cioni D, Saba L, Neri E. A deep look into radiomics. *Radiol Med*. 2021;126:1296-1311.

24. Kikinis R, Pieper SD, Vosburgh KG. 3D slicer: a platform for subject-specific image analysis, visualization, and clinical support. In: Jolesz FA, ed. *Intraoperative Imaging and Image-Guided Therapy*. New York: Springer; 2014:277-289.

25. Krzyżewski RM, Kliś KM, Kucala R, et al. Intracranial aneurysm distribution and characteristics according to gender. *Br J Neurosurg*. 2018;32:541-543.

26. Zuurbier CCM, Molenberg R, Mensing LA, et al. Sex difference and rupture rate of intracranial aneurysms: an individual patient data meta-analysis. *Stroke*. 2022;53:362-369.

27. Bonekamp D, Kohl S, Wiesenfarth M, et al. Radiomic machine learning for characterization of prostate lesions with MRI: comparison to ADC values. *Radiology*. 2018;289:128-137.

28. Acar E, Leblebici A, Ellidokuz BE, Başbınar Y, Kaya G. Machine learning for differentiating metastatic and completely responded sclerotic bone lesion in prostate cancer: a retrospective radiomics study. *Br J Radiol*. 2019;92:20190286.

29. Aerts HJ, Velazquez ER, Leijenaar RT, et al. Decoding tumour phenotype by noninvasive imaging using a quantitative radiomics approach. *Nat Commun*. 2014;5:4006.

30. Fan Y, Jiang S, Hua M, Feng S, Feng M, Wang R. Machine learning-based radiomics predicts radiotherapeutic response in patients with Acromegaly. Original research. *Front Endocrinol (Lausanne)*. 2019;10:588.

31. Futami K, Kitabayashi T, Sano H, et al. Inflow jet patterns of unruptured cerebral aneurysms based on the flow velocity in the parent artery: evaluation using 4D flow MRI. *AJNR Am J Neuroradiol*. 2016;37:1318-1323.

32. Detmer FJ, Chung BJ, Mut F, et al. Development of a statistical model for discrimination of rupture status in posterior communicating artery aneurysms. *Acta Neurochir (Wien)*. 2018;160:1643-1652.

33. Chung BJ, Mut F, Putman CM, et al. Identification of hostile hemodynamics and geometries of cerebral aneurysms: a case-control study. *Am J Neuroradiol*. 2018;39:1860-1866.

34. Schnell S, Ansari SA, Vakil P, et al. Three-dimensional hemodynamics in intracranial aneurysms: influence of size and morphology. *J Magn Reson Imaging*. 2014;39:120-131.

35. Lauric A, Hippelheuser JE, Malek AM. Moments of intra-dome velocity distribution as robust predictors of rupture status in cerebral aneurysms. *World Neurosurg*. 2022;158:e334-e343.

36. Detmer FJ, Lückehe D, Mut F, et al. Comparison of statistical learning approaches for cerebral aneurysm rupture assessment. *Int J Comput Assist Radiol Surg*. 2020;15:141-150.

37. Asari S, Ohmoto T. Natural history and risk factors of unruptured cerebral aneurysms. *Clin Neurol Neurosurg*. 1993;95:205-214.

38. Chien A, Sayre J, Viñuela F. Comparative morphological analysis of the geometry of ruptured and unruptured aneurysms. *Neurosurgery*. 2011;69:349-356.

IRB approval: This research was approved by Tufts Health Sciences Campus Institutional Review Board (IRB# 9035). Patient consent was waived because of the retrospective nature of the study not impacting patient clinical care.

Conflict of interest statement: The content of this manuscript, in part or in full, has not been published elsewhere in any form. I, Adel Malek, certify that this manuscript is a unique submission and is not being considered for publication with any other source in any medium. There is no declaration of interest to report. There are no sources of funding to report. The research is original and was conducted by the authors with significant contribution from each. This study was approved by Tufts Health Sciences Campus Institutional Review Board. We thank you for your assistance.

Received 7 October 2025; accepted 26 October 2025

Citation: World Neurosurg. (2026) 205:124602. http://doi.org/10.1016/j.wneu.2025.124602

*Journal homepage: **www.journals.elsevier.com/world-neurosurgery***

*Available online: **www.sciencedirect.com***

1878-8750/© 2025 The Author(s). Published by Elsevier Inc. This is an open access article under the CC BY license (http://creativecommons.org/licenses/by/4.0/).